

# The radio spectra of reddened 2MASS QSOs: evidence for young radio jets

A. Georgakakis<sup>2,1\*</sup>, M. Grossi<sup>3,4</sup>, J. Afonso<sup>3,4</sup>, A. M. Hopkins<sup>5</sup>

<sup>1</sup>*National Observatory of Athens, I. Metaxa & V. Paulou, Athens 15236, Greece*

<sup>2</sup>*Max-Planck-Institut für extraterrestrische Physik, Giessenbachstrasse 1, D-85748, Garching bei München, Germany*

<sup>3</sup>*Observatório Astronómico de Lisboa, Faculdade de Ciências, Universidade de Lisboa, Tapada da Ajuda, 1349-018 Lisbon, Portugal*

<sup>4</sup>*Centro de Astronomia e Astrofísica da Universidade de Lisboa, Lisbon, Portugal*

<sup>5</sup>*Australian Astronomical Observatory, P.O. Box 296, Epping, NSW 1710, Australia*

15 September 2021

## ABSTRACT

Multifrequency radio continuum observations (1.4–22 GHz) of a sample of reddened QSOs are presented. We find a high incidence (13/16) of radio spectral properties, such as low frequency turnovers, high frequency spectral breaks or steep power-law slopes, similar to those observed in powerful compact steep spectrum (CSS) and gigahertz-peaked spectrum (GPS) sources. The radio data are consistent with relatively young radio jets with synchrotron ages  $\lesssim 10^6 - 10^7$  yr. This calculation is limited by the lack of high resolution (milli-arcsec) radio observations. For the one source in the sample that such data are available a much younger radio age is determined,  $\lesssim 2 \times 10^3$  yr, similar to those of GPS/CSS sources. These findings are consistent with claims that reddened QSOs are young systems captured at the first stages of the growth of their supermassive black holes. It also suggests that expanding radio lobes may be an important feedback mode at the early stages of the evolution of AGN.

**Key words:** galaxies: active – galaxies: quasars: general – galaxies: jets – ISM: jets and outflows – radio continuum: general

## 1 INTRODUCTION

In the last few years an increasing body of observations points to an intimate relation between the formation of galaxies and the growth of the supermassive black holes (SMBH) at their centres (e.g. Ferrarese & Merritt 2000; Gebhardt et al. 2000). The nature of the interplay between the two components is still not well understood, although important for understanding both the star-formation and accretion history of the Universe.

The large energy output of QSOs relative to the binding energy of their hosts (e.g. Silk & Rees 1998) and the strong outflows observed in many of these systems (e.g. Reichard et al. 2003), motivated analytical calculations which proposed AGN feedback as the link between the formation of SMBH and the assembly galaxies (Silk & Rees 1998; Fabian 1999; King 2003, 2005). These studies suggest that the energy released by the central engine has a strong impact on the interstellar medium thereby affecting the evolutionary path of the host galaxy. These results are broadly supported by numerical simulations, which assume various AGN feedback mechanisms and different conditions under which SMBH grow (e.g. Di Matteo et al. 2005; Debuhr et al. 2010, 2011). The general picture emerging from the numerical simulations is that SMBHs

and stars form almost simultaneously as the result of gas inflows triggered by either major mergers (e.g. Springel et al. 2005), disk instabilities (Hopkins & Quataert 2010; Bournaud et al. 2011) or shocks in recycled gas from the winds of evolved stars (Ciotti & Ostriker 2007). The early stages of SMBH growth in all those models take place behind dust and gas cocoons, which at later times are blown away by some form of AGN related feedback mechanism. This allows the central engine to shine unobscured for a short period of time, before it runs out of fuel and switches off itself.

This generic evolutionary scheme, first put forward by Sanders et al. (1988), has been shown to be in broad agreement with observations of AGN and galaxies (e.g. Hopkins et al. 2008; Degraf et al. 2010, 2011). Nevertheless many of the details remain to be fully understood. A number of studies for example, debate the role and relative importance of different feedback modes, e.g. photoionisation, radiation pressure, bubbles, winds or jets (e.g. Hambrick et al. 2011, and references therein). Hopkins & Elvis (2010) propose a two stage feedback scheme, in which AGN first drive outflows in the hot/warm ISM, which in turn affect cold gas clouds by deforming them and hence substantially increasing their cross section to ionisation and radiation pressure from the central engine. The overall effect of this scenario is a reduction by almost 1 dex in the fraction of the AGN energy that needs to be deposited to the ISM to expel the gas of the host galaxy and regulate the formation of stars.

\* email: age@mpe.mpg.de

Recent studies also highlight the efficiency of starbursts for depleting the nuclear gas reservoirs of galaxy mergers, thereby substantially relaxing the requirements for AGN feedback for quenching star-formation (e.g. Cen 2011; Hopkins 2011).

AGN captured at an early stage of their evolution, when feedback processes are expected to be close to their peak, are excellent laboratories for testing these ideas and advancing our understanding on the interplay between the formation of SMBH and their hosts. Reddened QSOs, first identified in 2MASS (Two Micron All Sky Survey; Cutri et al. 2001; Wilkes et al. 2002; White et al. 2003; Glikman et al. 2007), are believed to represent young AGN. Key properties of this population which are consistent with the youth scenario include (i) red continua most likely associated with dust in the host galaxy (e.g. White et al. 2003; Glikman et al. 2007; Urrutia et al. 2009; Georgakakis et al. 2009), (ii) a high incidence of morphological disturbances suggestive of recent mergers (Urrutia et al. 2008), (iii) optical spectroscopic signatures for fast outflows in the warm phase of the interstellar medium (Urrutia et al. 2009), (iv) enhanced star-formation rates relative to UV bright QSOs (Georgakakis et al. 2009). All these findings are consistent with the scenario that reddened QSOs are observed shortly before or during the blow-out of their natal cocoon of dust and gas, i.e. at the stage where AGN feedback is close to its peak.

In Georgakakis et al. (2009) a higher radio detection rate was found for reddened QSOs compared to UV bright ones. First, this suggests that expanding radio lobes may play an important role at the early stages of SMBH growth. Second, by determining the synchrotron age of the electron population responsible for the jets one can set additional independent constraints to the youth scenario for reddened QSOs. The typical characteristics of young radio sources are compact radio sizes (less than few tens of kpc), radio spectra which show a turnover at low frequencies (attributed to synchrotron self-absorption or free-free absorption) and/or a double power-law distribution with relatively flat power-law slope at centimetre wavelengths ( $\alpha \approx 0.7$ , where the flux density at frequency  $\nu$  is  $S_\nu \propto \nu^{-\alpha}$ ) followed by a steepening at higher frequencies (O’Dea 1998). In the standard theory of synchrotron emission from expanding lobes (Kardashev 1962), spectral indices steeper than the canonical value of 0.7 are attributed to spectral aging. In this picture the break frequency, at which the slope of the power-law spectrum steepens, decreases with the time elapsed since the formation of the source as  $\nu_{br} \propto t^{-2}$ . The shape of the radio spectrum can therefore constrain the age of the jet.

This paper presents VLA (Very Large Array) and EVLA (Expanded Very Large Array) continuum observations in the frequency range 1.4–22 GHz of reddened QSOs selected from the literature. This multifrequency dataset is used to (i) constrain the overall shape of the radio spectra of reddened QSOs to search for features indicative of young radio jets (e.g. spectral breaks, low frequency turnovers) and (ii) estimate the break frequency  $\nu_{br}$  to use it as an age indicator. Additionally by constraining the radio spectra of reddened QSOs one can place them in the context of the population of compact steep spectrum (CSS) and gigahertz-peaked spectrum (GPS) radio sources. These objects are proposed to host young and expanding radio lobes (e.g. O’Dea 1998; Murgia et al. 1999), which are likely to have a strong impact on the ISM of their parent galaxies (e.g. Holt et al. 2011). Throughout the paper we adopt  $H_0 = 70 \text{ km s}^{-1} \text{ Mpc}^{-1}$ ,  $\Omega_M = 0.3$  and  $\Omega_\Lambda = 0.7$ .

## 2 OBSERVATIONS

The reddened QSOs followed with radio continuum observations at the VLA and EVLA are selected from the samples of Urrutia et al. (2009) and Georgakakis et al. (2009). These studies combined the 2MASS in the near-infrared and the Sloan Digital Sky Survey (SDSS) in the optical to select sources with red optical/near-infrared colours (i.e.  $R - K > 5$ ,  $J - K > 1.3$  mag in Urrutia et al. 2009;  $R - K > 5$ ,  $J - K \gtrsim 2$  mag in Georgakakis et al. 2009). The sample of Urrutia et al. (2009) also includes pre-selection of 2MASS sources with radio counterparts in the FIRST survey (Faint Images of the Radio Sky at Twenty-Centimeters, Becker et al. 1995). The 2MASS reddened QSOs targeted by our VLA and EVLA programmes are listed in Tables 1 and 2 respectively. They are selected to have radio (1.4 GHz) flux densities  $S_{1.4} \gtrsim 5 \text{ mJy}$  in the FIRST survey.

### 2.1 VLA data

Multi-frequency (1.4, 4.85, 8.4 and 22 GHz) simultaneous observations of the sources listed in Table 1 were carried out at the VLA in snapshot mode between May and August 2009. The VLA configurations changed during that period from CnB to C. Targets 2MASSQSO 10, F2MS0832+050, F2MS0932+385 were observed in the CnB configuration with the remainder observed in the C configuration. The dwell time in the L (1.4 GHz), C (4.85 GHz) and X (8.4 GHz) bands was 30 s. The targets were bracketed by observations in the same frequency of a nearby ( $< 10$  deg) phase calibrator. In the K-band (22 GHz) fast switching phase calibration was used to minimise phase variations. A cycle time of 100 seconds (70 sec on source, 30 sec on calibrator) and a dwell time of 5 min was adopted. Observations in the K-band were preceded by pointing observations in the X-band of the secondary calibrator. This is to minimise pointing errors which can significantly degrade the sensitivity in the K-band as the a priori pointing can be off by a large fraction of the primary beam in that band. Primary flux calibrators (3C147 or 3C286) were observed in all bands at the beginning of the multifrequency observations sequence of each target. Source F2MS 1618+350 and F2MS 1540+492 lack 1.4 GHz observations, while F2MS 1615+ 031 has not been observed at 22 GHz.

The data were reduced using the Astronomical Image Processing System (AIPS) maintained by NRAO and following standard reduction procedures. The secondary flux calibrators close to the targets were used to track gains and phases of each antenna. The calibration solutions have been derived with the task CALIB and they have been applied to the targets with the task CLCAL. The K band data were self-calibrated using standard procedures to improve the image dynamic range and reduce the noise level. Typically one iteration of phase-only self-calibration was performed. Finally the task IMAGR, which includes the algorithm CLEAN, was used to deconvolve the images.

The final images noise levels range from 0.3 to 0.8 mJy/beam (L band), 0.2 to 0.3 mJy/beam (C and X bands) and 0.3 to 0.5 mJy/beam (K band). The Gaussian restoring beam FWHM (Full Width Half Maximum) varies for each set of observations at each band. The typical beam sizes are approximately  $19'' \times 15''$ ,  $5'' \times 4''$ ,  $3'' \times 2''$  and  $1'' \times 0''.8$ , at 1.4, 4.8, 8.4 and 22 GHz respectively. The linear extent of the beam size of the highest spatial resolution radio image (22 GHz and if not available 8 GHz) at the redshift of each source is listed in Table 1. Flux densities have been measured by fitting Gaussians to the source profiles, using the AIPS task JM-

FIT. The results are presented in Table 1. That table also lists the rest-frame 5 GHz radio power of each reddened QSO.

For sources F2MS 1540+492, F2MS 1618+350, which lack 1.4 GHz observations in our VLA program, we use the 1.4 GHz flux densities estimated by the FIRST and Glikman et al. (2007) respectively. For source F2MS 1618+350 the FIRST and Glikman et al. (2007) 1.4 GHz flux densities differ by a factor of about 2. This discrepancy may be because of variability, extended emission which is resolved out by the FIRST data or calibration problems. Our data at higher frequencies (4.8, 8.4, 22 GHz) do not show extended radio emission. Glikman et al. (2007) have also determined the 8.4 GHz flux density of F2MS 1618+350, which is in good agreement with our estimate. This suggests that any biases because of source variability between the two observation epochs are small. We therefore choose to use the Glikman et al. (2007) 1.4 GHz flux density for F2MS 1618+350. It is noted that for the majority of our sample sources the 1.4 GHz densities estimated by FIRST and our observations typically agree within about 30 per cent.

Also, all sample sources, except F2MS 1618+3502, are unresolved in the FIRST or our VLA observations, suggesting sizes smaller than a few arcseconds. Source F2MS 1618+3502 shows two jets extending out to about 20 arcsec (115 kpc) from a radio bright core. Another 2MASS QSOs in Table 1, F2MS1030+5806, has been observed at milli-arcsec resolution at 5 GHz. The data are from the VLBA Imaging and Polarization Survey (VIPS) presented by Helmboldt et al. (2007). This source has a very compact radio morphology with a small scale (few milli-arcsec) radio jet with linear size at the redshift of the source of about 100 pc.

## 2.2 EVLA data

The EVLA data were obtained in snapshot mode at the L, C, X, and K bands between the 13th and the 30th of May 2010, in the D configuration. Observations were carried out in two contiguous, 128-MHz IF bands, each divided into 64 channels, and centred at 1348 and 1860 MHz (L-band), 4896 and 5024 MHz (C-band), 8396 and 8524 MHz (X-band), 22396 and 22524 GHz (K-band). Observations at 22 GHz have been carried out in the fast switching phase calibration mode to minimise phase variations.

The EVLA data were reduced using the Common Astronomy Software Applications (CASA) package release 3.0.2, maintained by NRAO and following the standard reduction procedure. Bandpass and flux density calibration were performed using the primary flux calibrators close to the targets (3C147, 3C286). The amplitude scale was set according to the Perley-Butler coefficients derived from recent measurements at the EVLA. Amplitude and phase gains were derived for all calibrator sources, with the task GAINCAL, and they have been applied to the targets with the task APPLYCAL, while the final images were produced with the task CLEAN using a Briggs weighting. The EVLA K-band data did not need to be self-calibrated.

The final images noise levels range in the intervals 0.3-1 mJy/beam (L-band), 0.2-0.3 mJy/beam (C-band), 0.1-0.2 mJy/beam (X-band) and 0.06-0.2 mJy/beam (K-band). The Gaussian restoring beam FWHM slightly varies for each set of observations at each band. The typical beam size is  $1'.2 \times 0'.8$ ,  $20'' \times 14''$ ,  $11'' \times 9''$ ,  $4'' \times 3''$ , for the L, C, X and K band, respectively. The linear extent of the beam size at 22 GHz (highest spatial resolution) at the redshift of each source is listed in Table 2. Flux densities have been measured by fitting Gaussians to the source profiles, using the task IMFIT. In the L-band we chose to produce two independent images, one for each IF unit, instead of combining the data. This

is because of the wide separation of the central frequencies of the two IF bands (1348 and 1860 MHz). The results are presented in Table 2. That table also lists the rest-frame 5 GHz radio power of each reddened QSO.

Source F2MS0841+3604 has not been observed in the X-band. Also technical problems affected the L-band observations of F2MS0841+3604, F2MS0915+2418, F2MS1456+0114. As a result it was not possible to obtain reliable measurements at either 1.3 GHz or 1.8 GHz. For those sources the FIRST radio flux density at 1.4 GHz is adopted (see Table 2).

## 3 RADIO SPECTRA OF 2MASS QSOs

The radio Spectral Energy Distributions (SEDs) of 2MASS QSOs are shown in Figure 1. Table 3 presents the radio spectral indices  $\alpha_{1.4-4.8\text{GHz}}$ ,  $\alpha_{8.4-22\text{GHz}}$  between the frequencies 1.4/4.8 GHz and 8.0/22 GHz respectively, which provide a model independent way of investigating spectral features characteristic of young jets, e.g. spectral breaks and/or turnovers. Depending on the radio spectral index at low and high frequencies and the overall shape of the SEDs in Figure 1 the sources in the sample can be grouped into 3 broad categories. There are spectra for which the radio flux density (i) declines monotonically with increasing frequency, (ii) shows a peak at GHz frequencies and decreases at both lower and higher frequencies, (iii) remains nearly constant in the frequency range 1.4–22 GHz and cannot be placed into one of categories above. The classification scheme above is shown in Table 3. Class (iii) sources have radio spectra suggestive of free-free thermal emission typically found at QSO cores.

The radio SEDs of group (i) can be described by either a single or a double power-law. The data are first fit with single power-law model of the form  $S_\nu \propto \nu^{-\alpha}$ , where  $\alpha$  is the spectral index. The standard  $\chi^2$  minimisation method is adopted for the fits. For the calculation of the  $\chi^2$  we add to the formal uncertainties determined by the JMFIT of AIPS listed in Tables 1 and 2 an error corresponding to 5 per cent of the total flux. This is to account for uncertainties in the overall calibration of the radio observations. The goodness of fit of the model is determined by estimating the probability,  $P_{SPL}$ , of getting by chance the calculated  $\chi^2$  for the given degrees of freedom (typically 2). We choose to reject the single power-law model if  $P_{SPL} < 0.05$ . The results are shown in Table 3.

Sources for which the single power-law model does not provide a good fit to the data are also fit with a double power-law. The continuous injection model with no adiabatic losses (Kardashev 1962) is adopted. In this case the spectral indices are  $\alpha_{inj}$  (with a canonical value of about 0.7) below the break frequency ( $\nu_{br}$ ) and  $\alpha \approx \alpha_{inj} + 0.5$  above  $\nu_{br}$ . This model was chosen because it fits well the spectra of GPS/CCS sources (Murgia et al. 1999; Murgia 2003). The model has 3 free parameters ( $\nu_{br}$ ,  $\alpha_{inj}$ , normalisation) and requires at least 4 points in the radio SED. Source F2MS 1618+3502, which shows evidence for a spectral break in its radio SED, is not detected at 22 GHz. We choose not to fit this source with the double power-law model described above. The best-fit parameters values, minimum  $\chi^2$  and the probabilities of the goodness of fit,  $P_{DPL}$ , are listed in Table 3. The continuous injection model typically provides adequate fits to the radio spectra of 2MASS QSOs with  $\alpha_{inj} \approx 0.4 - 0.8$  and  $\nu_{br} \approx 4 - 7$  GHz. One exceptions is source F2MS 1341+3301 for which the steepening of the spectrum at high frequencies is more pronounced than that assumed by the continuous injection model ( $\alpha \approx \alpha_{inj} + 0.5$ ).

Our analysis shows that more than half of the sources in the

sample (9/16) show deviations from the single power-law SED model and their radio spectra can be better described by (i) a double power-law with a steeper high frequency index or (ii) a turnover at low frequencies. These properties are consistent with those of powerful ( $P_{5\text{ GHz}} \gtrsim 10^{27}$  W/Hz) GPS sources (e.g. O’Dea 1998, Murgia et al. 1999, 2003, Randall et al. 2011). This population is also characterised by compact radio sizes, typically  $\lesssim 1$  kpc (O’Dea et al. 1998). The radio data presented in this paper set only weak limits on the physical extent of the radio jets. All reddened QSOs with GPS radio spectral characteristics appear unresolved in the VLA/EVLA images. At the resolution of those observations ( $\approx 1$  and 4 arcsec at 22 GHz respectively) the upper limits on the size of the radio emitting region are in the range 5-30 kpc (see Tables 1 and 2). With the present dataset it is therefore not possible to comment on the compactness of the radio sources of 2MASS QSOs relative to GPS sources.

For the reddened QSOs in the sample that can be described by a single power-law (4/16) our analysis yields steep spectral slopes,  $\alpha \approx 1$ . These sources are also unresolved in the VLA/EVLA images indicating radio size upper limits  $\lesssim 30$  kpc (see Tables 1 and 2). Both these properties are similar to those of CSS sources which show steep radio spectra and are typically confined within the extent of their host galaxies (O’Dea 1998; Randall et al. 2011).

We conclude that the majority of reddened QSOs studied in this paper (13/16) have radio spectral properties typical to those of powerful ( $P_{5\text{ GHz}} \gtrsim 10^{27}$  W/Hz) GPS/CSS sources, which are believed to host young and expanding radio jets. This is interesting because at bright fluxes the GPS/CSS population represents only about 20-30 per cent of radio selected samples (O’Dea et al. 1998). We caution however, that this fraction has not been determined for QSOs with radio emission at the mJy flux density levels of the present sample.

For those 2MASS QSOs for which the continuous injection model provides adequate fits to their radio spectra, the break frequency,  $\nu_{\text{break}}$ , listed in Table 3 can be used to estimate their synchrotron ages (e.g. Murgia et al. 1999; Drake et al. 2004a)

$$t_{\text{syn}} = 0.045 B^{-3/2} [\nu_{\text{br}} (1+z)], \quad (1)$$

where  $B$  is the magnetic field and  $z$  the source redshift. For this calculation we will assume the equipartition value for the magnetic field (e.g. Pacholczyk 1970; Duric 1991)

$$B = [6\pi (1+k) c_{12} V^{-1} L]^{2/7}, \quad (2)$$

where  $k$  is the heavy element to particle ratio,  $V$  is the volume,  $L$  is the synchrotron luminosity between frequencies  $\nu_1$ ,  $\nu_2$  and  $c_{12}$  is a constant which depends on  $\nu_1$  and  $\nu_2$  and the spectral index  $\alpha_{inj}$  of the radio SED (e.g. Irwin et al. 1999). The volume of the source is estimated from the highest resolution data available, which in most cases are the 22 GHz observations. In the absence of milli-arcsec radio data for the majority of the sources, this is an upper limit as 2MASS QSOs are typically unresolved in arcsec scale radio observations. We use  $k = 0$ ,  $\nu_1 = 100$  MHz and  $\nu_2 = 100$  GHz, which are often adopted in the literature. The estimated synchrotron ages are somewhat sensitive (factor of a few) to those parameters.

Table 4 lists the synchrotron ages and luminosities as well as the magnetic fields for those sources in the sample that an estimate of  $\nu_{\text{br}}$  can be obtained from the observations. In addition to sources with radio spectra better described by a double power-law, we also estimate  $t_{\text{syn}}$  for 2MASS QSOs F2MS1540+4923 and F2MS1030+5806. The former is described by a single power-law with  $\alpha \approx 0.8$ , similar to the canonical value of  $\approx 0.7$  expected

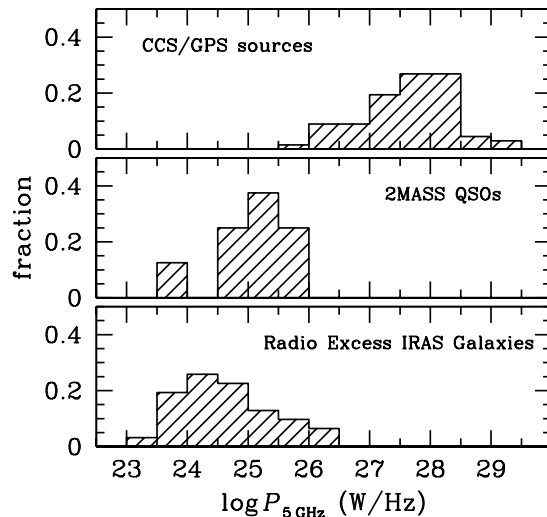


**Figure 2.** Radio (5 GHz) power distribution for GPS/CSS sources (O’Dea & Baum 1997; top panel), reddened QSOs (middle panel) and radio excess IRAS galaxies (Drake et al. 2004a; bottom panel). The radio powers of GPS/CSS are from O’Dea & Baum (1997). For radio excess IRAS galaxies the radio multifrequency radio data presented by Drake et al. (2004a) are used to interpolate and estimate the rest-frame 5 GHz radio power. The same approach is used for reddened QSOs.

for a zero age electron population (Kardashev 1962). Therefore the break frequency for this object likely lies above 22 GHz at the observer’s frame. The radio spectrum of F2MS1030+5806 shows a turnover below about 5 GHz and therefore cannot be fit with the continuous injection model. However, the spectral index of this source at high frequencies is  $\alpha_{8.4-22\text{GHz}} = 0.52 \pm 0.01$ , close to the canonical synchrotron slope and similar to the injection slopes estimated in Table 3 for others 2MASS QSOs with spectra better described by the continuous injection model. It is thus likely that  $\nu_{\text{br}} > 22$  GHz for this source.

The upper limits of the synchrotron ages of 2MASS QSOs are typically of the order of few  $10^6$  yrs. For comparison extended radio galaxies typically have  $t_{\text{syn}} \approx 10^7 - 10^8$  yrs (e.g. Klein et al. 1995; Parma et al. 1999), while GPS/CSS sources are believed to be much younger,  $t_{\text{syn}} = 10^3 - 10^5$  yr (e.g. Murgia et al. 1999). The main limitation in the calculation of synchrotron ages for 2MASS QSOs is the lack of high resolution radio data. For the one source in the sample (F2MS1030+5806) that such observations are available, much younger ages are estimated,  $t_{\text{syn}} < 2000$  yr, similar to GPS/CSS sources. It is therefore likely that the upper limits in  $t_{\text{syn}}$  listed in Table 4 are conservative. In any case, the similarity of the radio spectral properties of GPS/CSS sources and 2MASS QSOs supports the youth scenario for the latter population.

#### 4 RADIO VS MULTIWAVELENGTH PROPERTIES

Next we study the multiwavelength properties of the reddened QSOs in Table 3 in relation to their radio spectral characteristics. This is to investigate on a source to source basis if the young radio jet scenario is supported by observations at other wavelengths.

Four sources in Table 3 have been investigated by Urrutia et al. (2008) for Broad Absorption Lines (BALs) blueward of the

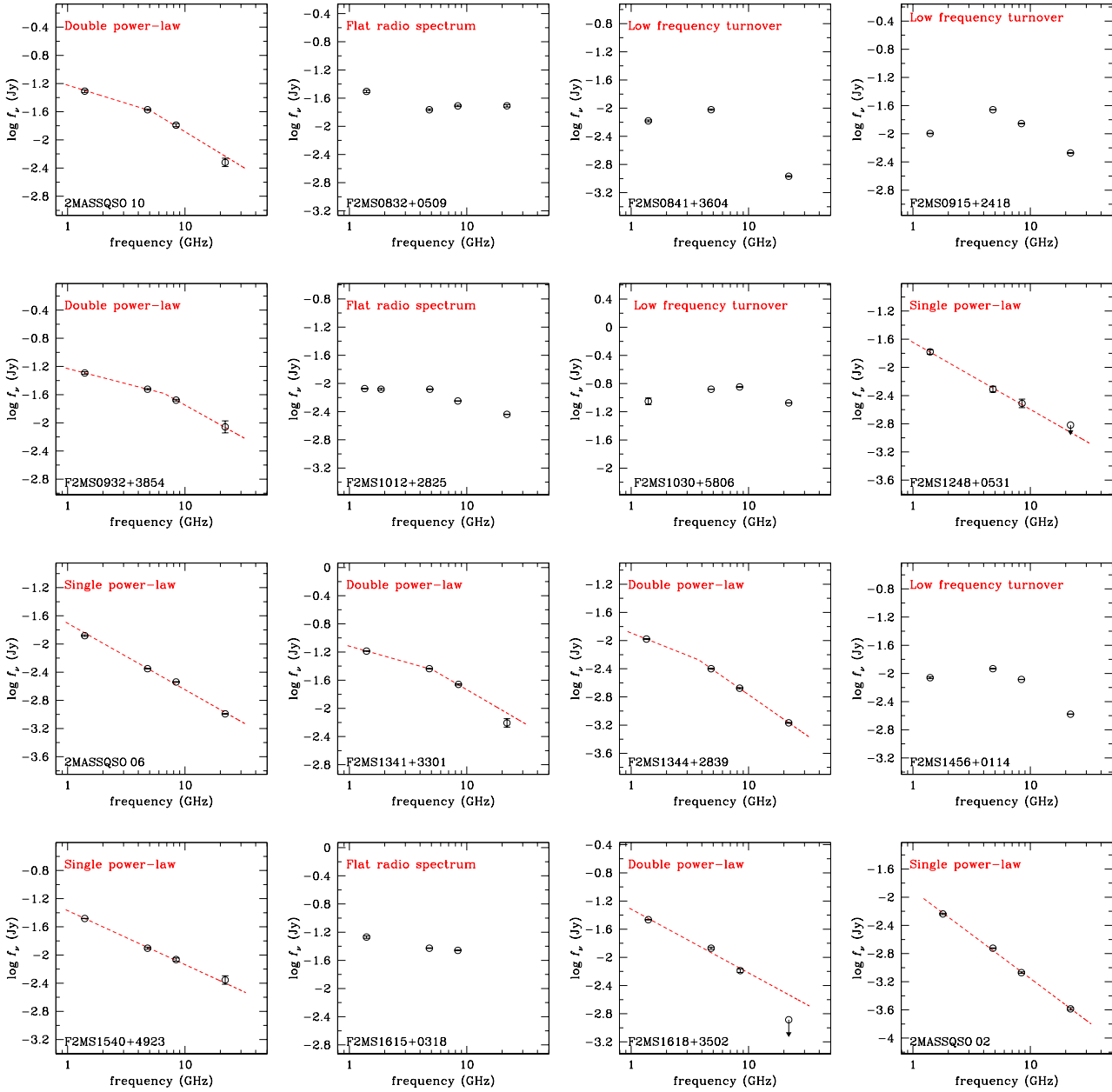


**Figure 1.** Radio spectra of reddened QSOs in the frequency range 1.4–22 GHz. Sources are ordered in a way that their Right Ascension is increasing from left to right and from top to bottom. Upper limits in radio flux density are shown with an arrow pointing downward. The y-axis in all plots is scaled to span the range  $\pm 1.5$  dex around the flux density of each source at 4.8 GHz. The dashed lines correspond to the best-fit single power-law or continuous injection model with no adiabatic losses (Kardashev 1962). The latter is plotted for sources for which a single power-law provides a poor fit to the data ( $P_{SPL} < 0.05$ , see Table 3). Sources with a turnover at low frequencies cannot be fit by the continuous injection model. Also, Source FM2S 1618+3502, which shows evidence for a spectral break in its radio spectrum (see  $\alpha_{1.4-4.8\text{GHz}}$ ,  $\alpha_{8.4-22\text{GHz}}$  in Table 3), is not detected at 22 GHz. This source is not fit with the continuous injection model and only. For that source only the single power-law model is shown. In the fit process the 22 GHz upper limit is not used. The label on the top of each panel indicates the spectral characteristics of each source (single power-law, double power-law, low frequency turnover or flat radio spectrum).

MgII 2800Å emission. Two of them are classified as Low Ionisation BALs (LoBALs; F2MS 1344+2839, F2MS 1456+0114), the class of BALs which are proposed to represent an early evolutionary stage in the quasar lifetime (e.g. Becker et al. 2000; Trump et al. 2006). Interestingly both those sources also have radio spectra similar to GPS/CSS sources, consistent with the youth scenario. Moreover, the two sources that are characterised as non-BALs by Urru-

tia et al. (2009; F2MS 0832+0509, F2MS 1012+2825) have flat radio spectra, indicative of thermal emission often observed at QSO cores.

Another source in our sample that shows evidence for outflows in the form of double-peaked narrow emission lines separated by  $600 \text{ km s}^{-1}$  (Urrutia et al. 2008) is 2MASSQSO 10. The radio

spectrum of that system is better described by the continuous injection model, suggestive of young radio jets.

HST observations are available for reddened QSOs 2MASSQSO10, F2MS0841+3604, F2MS0915+2418 and F2MS1012+2825 (Urrutia et al. 2008). Those sources which have radio spectral properties similar to those of GPS/CSS sources (2MASSQSO10, F2MS0841+3604, F2MS0915+2418) also show highly disturbed optical morphologies indicative of ongoing mergers. The one source that shows the least disturbed optical light profile is F2MS1012+2825, which is also characterised by a flat radio spectrum. Although HST reveals two nuclei with separation of only 0.15 arcsec (1.2 kpc), the optical isophotes of this object follow a smooth elliptical light profile.

The reddened QSOs in Table 1 for which X-ray data are available (Urrutia et al. 2005, F2MS0841+3604, F2MS0915+2418 and F2MS1012+2825) typically show hard X-ray spectra, indicative of obscured ( $N_{\text{H}} \gtrsim 10^{22} \text{ cm}^{-2}$ ) AGN. We do not find any obvious relation between their X-ray properties and radio spectra.

Overall the optical spectra and morphologies of the reddened QSOs with radio properties suggestive of young radio jets are also consistent with objects in the process of formation. Two of the sample sources with flat radio spectra do not share those properties.

## 5 DISCUSSION

We find that a large fraction of reddened QSOs show either spectral breaks and/or turnovers at low frequencies (9/16) or steep radio spectra and relatively small radio sizes (4/16). Similar spectral characteristics are observed in GPS/CSS radio sources and are interpreted as evidence for young ( $10^3 - 10^5$  yrs) and expanding radio jets (O’Dea & Baum 1997; O’Dea 1998; Murgia et al. 1999; Murgia 2003; Randall et al. 2011). Compared to that population however, 2MASS QSOs are underluminous at radio frequencies (5 GHz, see Tables 1, 2) by at least few orders of magnitude. This is demonstrated in Figure 2 showing the distribution of 5 GHz radio powers for our sample and GPS/CSS sources (O’Dea & Baum 1997). This is likely because of differences in both the flux density limits ( $S_{1.4} \gtrsim 5 \text{ mJy}$  for 2MASS QSOs vs  $S_4 \gtrsim 1 \text{ Jy}$  for GPS/CSS sources) and the redshift distributions (median redshift of 0.74 for 2MASS QSOs vs 0.9 for GPS/CSS sources) of the two samples. In any case, the 2MASS QSOs presented in this paper appear to be low power analogues of GPS/CCS sources.

The comparison between the radio properties of 2MASS QSOs and GPS/CSS sources should also take into account the size of the radio emitting region in the two populations. Although CCS sources extend over tens of kpc, the GPS radio population is more compact ( $\lesssim 1 \text{ kpc}$ ; O’Dea et al. 1998). The VLA/EVLA observations presented in this paper lack the spatial resolution to set interesting limits on the size of the radio emitting region of 2MASS QSOs. Nevertheless, for the one 2MASS QSOs in our sample (F2MS1030+5806) that tight constraints on the jet size are available from milli-arcsec resolution observations, both its extent and inferred radio age are consistent with those of GPS sources. It is interesting that this source also has the highest radio power in the sample,  $P_{5 \text{ GHz}} = 10^{26} \text{ W/Hz}$  (see Table 1).

The high incidence of radio spectral properties suggestive of young radio jets among reddened QSOs is consistent with suggestions that these systems represent an early and brief stage of the growth of SMBHs (Hopkins et al. 2008; Urrutia et al. 2008, 2009; Georgakakis et al. 2009). In this picture reddened QSOs are the predecessors of UV/optically bright type-I AGN. They are captured at

a critical time of their evolution during which the natal dust and gas cocoon that enshrouds the SMBH is blown away by some feedback process related to the energy output of the central engine.

Outflows in the ionised gas are indeed observed in reddened QSOs. For the high redshift ( $z \gtrsim 0.9$ ) subset of those sources, for which the Mg II 2800Å emission line lies within the optical spectroscopic window, a high fraction of low ionisation BALs is reported by Urrutia et al. (2009). The young radio jets found by our analysis may play an important role in driving these outflows. In the more radio luminous GPS/CSS sources, outflows also traced in the ionised or neutral gas (e.g. Holt et al. 2003, 2006, 2008, 2011; Morganti et al. 2005) and are proposed to be associated with the expanding powerful radio jets (Batcheldor et al. 2007). These findings coupled with the suggestion by Georgakakis et al. (2009) for a high fraction of radio detections among reddened QSOs compared to UV/optically bright ones, highlights the potential significance of radio jets as a feedback mechanism at the early stages of AGN evolution.

This is consistent with the two-stage feedback scheme proposed by Hopkins & Elvis (2010). They suggest that some AGN related process, which the evidence above suggests might be radio jets, first drives a wind in the warm/hot diffuse gas. Cold clouds are then deformed and shredded in the wake of this outflow, thereby effectively becoming more susceptible to pressure and ionisation from the QSO intense radiation field. The net result of this process is a significant reduction of the initial AGN energy output that needs to couple with the ISM to blow away or destroy the cold gas of its host galaxy, in better agreement with recent observations (e.g. Holt et al. 2006, 2011).

Another population of sources which are also found to include a high fraction of relatively young radio jets ( $< 10^6$  yrs) are Radio Excess IRAS Galaxies (Drake et al. 2003, 2004a). Given the similarities in the radio properties of Radio Excess IRAS Galaxies and reddened 2MASS QSOs it is interesting to compare the multiwavelength properties of the two populations.

Radio Excess IRAS Galaxies are selected to have radio emission above the expectation from the radio/far-infrared correlation for star-formation (Drake et al. 2003). The majority of these sources (70 per cent) are hosted by galaxies which either show disturbed optical morphology or have nearby companions suggestive of tidal interactions (Drake et al. 2004b). This is similar to 2MASS QSOs, a large fraction of which show morphological evidence for mergers (Urrutia et al. 2008). Studies of the optical spectra of Radio Excess IRAS Galaxies (Buchanan et al. 2006) show a large fraction of post-starburst stellar continua, indicating recently terminated ( $< 1 \text{ Gyr}$ ) star-formation activity. In reddened QSOs, the optical spectra have a significant contribution from the central engine, and therefore the identification of host galaxy spectral features is difficult. Nevertheless, Georgakakis et al. (2009) studied the infrared properties of reddened 2MASS QSOs and found evidence for enhanced star-formation compared to optically selected QSOs. Blueshifts between the [O III] 5007Å line and the broad emission lines are also observed in Radio Excess IRAS Galaxies and are interpreted as evidence for interactions between the radio jet and the surrounding interstellar medium (Buchanan et al. 2006). Similarly, outflows in the warm ISM are observed in reddened QSOs (Urrutia et al. 2009). Figure 2 shows that the two populations have similar radio power distributions at 5 GHz, with Radio Excess IRAS Galaxies having a lower median. This can be attributed to the different redshift distributions of the two samples, with medians of 0.15 and 0.74 for Radio Excess IRAS Galaxies and 2MASS QSOs, respectively.

**Table 1.** The sample of reddened QSOs observed by VLA

ID	$\alpha$ (J2000)	$\delta$ (J2000)	redshift	$S_{1.4\text{ GHz}}$ (mJy)	$S_{4.8\text{ GHz}}$ (mJy)	$S_{8.4\text{ GHz}}$ (mJy)	$S_{22.0\text{ GHz}}$ (mJy)	$\log P_{5\text{ GHz}}$ (W/Hz)	beam size (kpc)
(1)	(2)	(3)	(4)	(5)	(6)	(7)	(8)	(9)	(10)
2MASSQSO10	08:25:02.05	+47:16:51.96	0.804	$49.2 \pm 2.2$	$26.8 \pm 0.6$	$16.2 \pm 0.8$	$4.8 \pm 0.7$	25.4	7.5
F2MS0832+0509	08:32:11.64	+05:09:01.04	1.070	$31.3 \pm 1.2$	$17.2 \pm 0.5$	$19.5 \pm 0.5$	$19.5 \pm 0.8$	25.8	8.1
F2MS0932+3854	09:32:33.29	+38:54:28.12	0.506	$51 \pm 2$	$30.0 \pm 0.6$	$21.0 \pm 0.5$	$8.8 \pm 1.7$	25.2	6.1
F2MS1030+5806	10:30:39.62	+58:06:11.41	0.504	$89.0 \pm 9.5$	$132.0 \pm 0.5$	$142.0 \pm 0.5$	$84.32 \pm 0.72$	26.0	6.1
F2MS1248+0531	12:48:47.16	+05:31:30.79	0.740	$16.6 \pm 1.2$	$4.9 \pm 0.5$	$3.08 \pm 0.43$	$< 1.52$	24.6	21.9
F2MS1341+3301	13:41:08.11	+33:01:10.23	1.720	$65.1 \pm 0.6$	$36.6 \pm 0.4$	$21.9 \pm 0.5$	$6.2 \pm 0.9$	25.9	8.5
F2MS1540+4923	15:40:43.74	+49:23:23.89	0.696	$32.99 \pm 0.0$	$12.50 \pm 0.40$	$8.6 \pm 0.5$	$4.4 \pm 0.6$	25.0	7.1
F2MS1615+0318	16:15:47.90	+03:18:50.83	0.424	$54 \pm 2$	$37.4 \pm 0.4$	$34.8 \pm 0.5$	-	25.2	16.8
F2MS1618+3502	16:18:09.72	+35:02:08.53	0.446	$34.3 \pm 0.2$	$13.5 \pm 0.4$	$6.5 \pm 0.4$	$< 1.30$	24.6	17.1

The columns are: (1) Source ID as listed in Georgakakis et al. (2009) or Urrutia et al. (2009); (2) right ascension; (3) declination; (4) source redshift; (5) 1.4 GHz radio flux density in mJy. Sources F2MS1540+4923 and F2MS1618+3502 have not been observed at 1.4 GHz. The listed flux densities are from the FIRST survey (F2MS1540+4923) and Glikman et al. (2007; F2MS1618+3502); (6) 4.8 GHz radio flux density in mJy; (7) 8.4 GHz radio flux density in mJy; (8) 22.0 GHz radio flux density in mJy. Source F2MS1615+0318 has not been observed at this frequency because of technical problems; (9) Radio power at 5 GHz estimated by interpolating between the observed data points; (10) Linear size in kpc of the antenna beam at 22 GHz at the redshift of the source. For sources not detected or not observed at 22 GHz the 8 GHz beam size is listed. For unresolved sources (all but F2MS1618+3502, see section 2.1) this the upper limit of the extent of the radio emitting region.

**Table 2.** The sample of reddened QSOs observed by EVLA

ID	$\alpha$ (J2000)	$\delta$ (J2000)	redshift	$S_{1.3\text{ GHz}}$ (mJy)	$S_{1.8\text{ GHz}}$ (mJy)	$S_{4.8\text{ GHz}}$ (mJy)	$S_{8.4\text{ GHz}}$ (mJy)	$S_{22.0\text{ GHz}}$ (mJy)	$\log P_{5\text{ GHz}}$ (W/Hz)	beam size (kpc)
(1)	(2)	(3)	(4)	(5)	(6)	(7)	(8)	(9)	(10)	
F2MS0841+3604	08:41:04.98	+36:04:50.09	0.552	$6.6 \pm 0.2$	-	$9.5 \pm 0.2$	-	$1.08 \pm 0.02$	24.6	25.0
F2MS0915+2418	09:15:01.71	+24:18:12.24	0.842	$10.1 \pm 0.1$	-	$21.96 \pm 0.07$	$13.97 \pm 0.09$	$5.34 \pm 0.07$	25.4	30.5
F2MS1012+2825	10:12:30.49	+28:25:27.15	0.937	$8.5 \pm 0.1$	$8.3 \pm 0.2$	$8.3 \pm 0.1$	$5.64 \pm 0.04$	$3.64 \pm 0.03$	25.1	31.5
2MASSQSO06	13:40:39.68	+05:14:19.90	0.259	$12.9 \pm 0.3$	$13.4 \pm 0.3$	$4.46 \pm 0.03$	$2.89 \pm 0.03$	$1.02 \pm 0.01$	23.8	16.0
F2MS1344+2839	13:44:08.31	+28:39:31.97	1.770	$10.5 \pm 0.2$	-	$3.99 \pm 0.07$	$2.11 \pm 0.04$	$0.68 \pm 0.01$	25.0	33.8
F2MS1456+0114	14:56:03.09	+01:14:45.71	2.378	$8.7 \pm 0.2$	-	$11.68 \pm 0.06$	$8.21 \pm 0.04$	$2.64 \pm 0.02$	25.7	32.6
2MASSQSO02	20:56:29.76	-06:50:55.40	0.635	-	$5.8 \pm 0.1$	$1.89 \pm 0.02$	$0.85 \pm 0.02$	$0.26 \pm 0.01$	24.0	27.4

The columns are: (1) Source ID as listed in Georgakakis et al. (2009) or Urrutia et al. (2009); (2) right ascension; (3) declination; (4) source redshift; (5) 1.3 GHz radio flux density in mJy. Source F2MS1456+0114 has a nearby radio source which is not resolved by the EVLA L-band observations. The radio flux density at this frequency is from the FIRST. The L-band observations of F2MS0841+3604, F2MS0915+2418 suffered technical problems. The listed flux densities for those objects are from the FIRST. The 1.3 GHz flux density of 2MASSQSO02 could not be estimated; (6) 1.8 GHz radio flux density in mJy. The 1.8 GHz flux density of F2MS1344+2839 could not be estimated; (7) 4.8 GHz radio flux density in mJy; (8) 8.4 GHz radio flux density in mJy; (9) 22.0 GHz radio flux density in mJy; (9) Radio power at 5 GHz estimated by interpolating between the observed data points; (10) Linear size in kpc of the antenna beam at 22 GHz at the redshift of the source. This is the upper limit of the extent of the radio emitting region as all listed sources are unresolved in the EVLA images.

## 6 CONCLUSIONS

In summary the multifrequency radio observations (1.4-22 GHz) of reddened QSOs presented in this paper reveal a high fraction of spectral features (breaks and/or turnovers) suggestive of young ( $\lesssim 10^6$  yrs) radio jets. This is consistent with the youth scenario for reddened QSOs according to which they are systems captured at an early stage of the formation of their SMBHs. The evidence for young and expanding radio lobes coupled with claims for a higher fraction of radio detections among reddened QSOs (Georgakakis et al. 2009), suggest that feedback associated with radio jets may play an important role at the early phases of the evolution of AGN and their host galaxies. This supports the two stage feedback scheme suggested by Hopkins & Elvis (2010).

## 7 ACKNOWLEDGEMENTS

The authors would like to thank the referee, Joanna Holt, for constructive comments. AG acknowledges financial support from the Marie-Curie Reintegration Grant PERG03-GA-2008-230644. JA and MG gratefully acknowledge support from the Science and Technology Foundation (FCT, Portugal) through the research grant PTDC/CTE-AST/105287/2008. The National Radio Astronomy Observatory is a facility of the National Science Foundation operated under cooperative agreement by Associated Universities, Inc.

## REFERENCES

- Batcheldor D., Tadhunter C., Holt J., Morganti R., O’Dea C. P., Axon D. J., Koekemoer A., 2007, *ApJ*, 661, 70

**Table 3.** Radio spectral slopes

ID	$\alpha_{1.4\text{ GHz}}^{4.8\text{ GHz}}$	$\alpha_{8.5\text{ GHz}}^{22\text{ GHz}}$	class	SPL Parameters				DPL Parameters			GPS/CSS
				$\alpha$	$\chi^2$	$P_{SPL}$	$\nu_{break}$ (GHz)	$\alpha_{inj}$	$\chi^2$	$P_{DPL}$	
2MASSQSO10	$0.49 \pm 0.07$	$1.3 \pm 0.2$	(i)	$0.75^{+0.03}_{-0.02}$	27.0	$< 10^{-4}$	$5.1^{+1.1}_{-1.1}$	$0.52^{+0.06}_{-0.07}$	2.5	0.11	DPL
F2MS0832+0509	$0.49 \pm 0.07$	$0.00 \pm 0.09$	(iii)	–	–	–	–	–	–	–	–
F2MS0841+3604	$-0.30 \pm 0.06$	–	(ii)	–	–	–	–	–	–	–	LFT
F2MS0915+2418	$-0.63 \pm 0.06$	$1.00 \pm 0.07$	(ii)	–	–	–	–	–	–	–	LFT
F2MS0932+3854	$0.43 \pm 0.07$	$0.9 \pm 0.2$	(i)	$0.54^{+0.04}_{-0.04}$	6.7	0.035	$6.7^{+0.9}_{-0.9}$	$0.43^{+0.05}_{-0.05}$	0.1	0.75	DPL
F2MS1012+2825	$0.02 \pm 0.06$	$0.45 \pm 0.07$	(iii)	–	–	–	–	–	–	–	–
F2MS1030+5806	$-0.32 \pm 0.10$	$0.54 \pm 0.07$	(ii)	–	–	–	–	–	–	–	LFT
F2MS1248+0531	$1.0 \pm 0.1$	$> 0.73$	(i)	$0.96^{+0.07}_{-0.08}$	0.3	0.58	–	–	–	–	SPL
2MASSQSO06	$0.88 \pm 0.06$	$1.08 \pm 0.07$	(i)	$0.92^{+0.05}_{-0.04}$	5.3	0.07	–	–	–	–	SPL
F2MS1341+3301	$0.47 \pm 0.06$	$1.3 \pm 0.2$	(i)	$0.71^{+0.03}_{-0.03}$	37.8	$< 10^{-4}$	$5.1^{+0.5}_{-0.7}$	$0.47^{+0.02}_{-0.04}$	5.0	0.025	DPL
F2MS1344+2839	$0.79 \pm 0.06$	$1.18 \pm 0.08$	(i)	$0.97^{+0.03}_{-0.02}$	20.0	$< 10^{-4}$	$3.8^{+3.2}_{-1.2}$	$0.66^{+0.08}_{-0.08}$	0.04	0.84	DPL
F2MS1456+0114	$-0.24 \pm 0.06$	$1.18 \pm 0.07$	(ii)	–	–	–	–	–	–	–	LFT
F2MS1540+4923	$0.78 \pm 0.06$	$0.7 \pm 0.2$	(i)	$0.77^{+0.02}_{-0.02}$	0.6	0.74	–	–	–	–	SPL
F2MS1615+0318	$0.29 \pm 0.06$	–	(iii)	–	–	–	–	–	–	–	–
F2MS1618+3502	$0.76 \pm 0.06$	$> 1.7$	(i)	$0.88^{+0.04}_{-0.04}$	2.21	0.14	–	–	–	–	DPL
2MASSQSO02	$0.91 \pm 0.06$	$1.23 \pm 0.09$	(i)	$1.25^{+0.03}_{-0.04}$	2.52	0.28	–	–	–	–	SPL

The columns are: (1): Source ID; (2) spectral index  $\alpha_{1.4-4.8\text{GHz}}$  between the frequencies 1.4 and 4.8 GHz; (3) spectral index  $\alpha_{8.4-22\text{GHz}}$  between the frequencies 8.0 and 22 GHz respectively; (4) classification based on the spectral indices  $\alpha_{1.4\text{ GHz}}^{4.8\text{ GHz}}$ ,  $\alpha_{8.5\text{ GHz}}^{22\text{ GHz}}$  and the overall shape of the radio spectrum (see text for details); (5): best-fit spectral index for the single power-law model. The uncertainties correspond to the 68 per cent confidence level. For source F2MS1618+3502 only the 1.4–8.4 GHz data are used in the fit; (6)  $\chi^2$  of the best-fit single power-law model and degrees of freedom; (7) goodness of fit probability for the single power-law model for the estimated minimum  $\chi^2$  and the degrees of freedom. For sources with  $P_{SPL} < 0.05$  best-fit parameters for the continuous injection model (double power-law) are also estimated. In this case the additional columns are (8) best-fit and 68 per cent confidence level errors for the break frequency of the continuous injection model; (9) best-fit and 68 per cent confidence level errors for the low frequency spectral index of the continuous injection model; (10)  $\chi^2$  of the best-fit continuous injection model and number of degrees of freedom; (11) probability of goodness of fit; (11) marks sources with radio spectral features consistent with those of the GPS/CSS population. The acronyms indicate LFT: low frequency turnovers, DPL: double power-law and SPL: steep power-law spectrum.

**Table 4.** Synchrotron timescales

ID	source size (kpc)	$\nu_{break}$ (GHz)	$L_{syn}$ (erg/s)	$B_{min}$ ( $\mu\text{G}$ )	$t_{syn}$ (yr)
2MASSQSO10	$< 7.5$	5.1	$4.0 \times 10^{43}$	$> 34.2$	$< 2.3 \times 10^6$
F2MS0932+3854	$< 6.1$	6.7	$1.5 \times 10^{43}$	$> 28.4$	$< 3.0 \times 10^6$
F2MS1030+5806	0.06	$> 22.0$	$7.1 \times 10^{43}$	2500	$< 2.0 \times 10^3$
F2MS1341+3301	$< 8.5$	5.1	$7.6 \times 10^{44}$	$> 69.1$	$< 0.6 \times 10^6$
F2MS1344+2839	$< 33.8$	3.8	$7.0 \times 10^{43}$	$> 41.0$	$< 1.7 \times 10^6$
F2MS1540+4923	$< 7.1$	$> 22.0$	$8.3 \times 10^{42}$	$> 12.5$	$< 9.9 \times 10^6$

The columns are: (1): Source ID; (2): source size in the highest resolution radio data available. Those are typically the 22 GHz observations, except from source F2MS1030+5806 for which milli-arcsec scale radio data are available from Helmboldt et al. (2007); (3) best-fit break frequency of the continuous injection model; (4): synchrotron luminosity in erg/s between frequencies  $\nu_1 = 100\text{ MHz}$  and  $\nu_2 = 100\text{ GHz}$ ; (5): minimum energy (equipartition) magnetic field in  $\mu\text{G}$  (equation 2); (6): synchrotron timescale in years (equation 1)

Becker R. H., White R. L., Gregg M. D., Brotherton M. S., Laurent-Muehleisen S. A., Arav N., 2000, ApJ, 538, 72  
 Becker R. H., White R. L., Helfand D. J., 1995, ApJ, 450, 559  
 Bournaud F., Dekel A., Teyssier R., Cacciato M., Daddi E., Juneau S., Shankar P., 2011, ArXiv e-print 1107.1483  
 Buchanan C. L., McGregor P. J., Bicknell G. V., Dopita M. A., 2006, AJ, 132, 27  
 Cen R., 2011, arXiv:1102.0262  
 Ciotti L., Ostriker J. P., 2007, ApJ, 665, 1038  
 Cutri R. M., Nelson B. O., Kirkpatrick J. D., Huchra J. P., Smith P. S., 2001, in Bulletin of the American Astronomical Society, Vol. 33, Bulletin of the American Astronomical Society, pp.

829–

Debuhr J., Quataert E., Ma C.-P., 2011, MNRAS, 412, 1341  
 Debuhr J., Quataert E., Ma C.-P., Hopkins P., 2010, MNRAS, 406, L55  
 Degraf C., Di Matteo T., Springel V., 2010, MNRAS, 402, 1927  
 —, 2011, MNRAS, 413, 1383  
 Di Matteo T., Springel V., Hernquist L., 2005, Nature, 433, 604  
 Drake C. L., Bicknell G. V., McGregor P. J., Dopita M. A., 2004a, AJ, 128, 969  
 Drake C. L., McGregor P. J., Dopita M. A., 2004b, AJ, 128, 955  
 Drake C. L., McGregor P. J., Dopita M. A., van Breugel W. J. M., 2003, AJ, 126, 2237

- Duric N., 1991, in *Astronomical Society of the Pacific Conference Series*, Vol. 18, *The Interpretation of Modern Synthesis Observations of Spiral Galaxies*, N. Duric & P. C. Crane, ed., pp. 17–26
- Fabian A. C., 1999, *MNRAS*, 308, L39
- Ferrarese L., Merritt D., 2000, *ApJ*, 539, L9
- Gebhardt K., Bender R., Bower G., Dressler A., Faber S. M., Filippenko A. V., Green R., Grillmair C., Ho L. C., Kormendy J., Lauer T. R., Magorrian J., Pinkney J., Richstone D., Tremaine S., 2000, *ApJ*, 539, L13
- Georgakakis A., et al., 2009, *MNRAS*, 397, 623
- Glikman E., Helfand D. J., White R. L., Becker R. H., Gregg M. D., Lacy M., 2007, *ApJ*, 667, 673
- Hambrick D. C., Ostriker J. P., Naab T., Johansson P. H., 2011, *ArXiv e-prints* 1106.1405
- Helmboldt J. F., et al., 2007, *ApJ*, 658, 203
- Holt J., Tadhunter C., Morganti R., Bellamy M., González Delgado R. M., Tzioumis A., Inskip K. J., 2006, *MNRAS*, 370, 1633
- Holt J., Tadhunter C. N., Morganti R., 2003, *MNRAS*, 342, 227
- , 2008, *MNRAS*, 387, 639
- Holt J., Tadhunter C. N., Morganti R., Emonts B. H. C., 2011, *MNRAS*, 410, 1527
- Hopkins P. F., 2011, *ArXiv e-prints* 1101.4230
- Hopkins P. F., Elvis M., 2010, *MNRAS*, 401, 7
- Hopkins P. F., Hernquist L., Cox T. J., Kereš D., 2008, *ApJS*, 175, 356
- Hopkins P. F., Quataert E., 2010, *MNRAS*, 407, 1529
- Irwin J. A., English J., Sorathia B., 1999, *AJ*, 117, 2102
- Kardashev N. S., 1962, *Soviet Ast.*, 6, 317
- King A., 2003, *ApJ*, 596, L27
- , 2005, *ApJ*, 635, L121
- Klein U., Mack K.-H., Gregorini L., Parma P., 1995, *A&A*, 303, 427
- Morganti R., Tadhunter C. N., Oosterloo T. A., 2005, *A&A*, 444, L9
- Murgia M., 2003, *PASA*, 20, 19
- Murgia M., Fanti C., Fanti R., Gregorini L., Klein U., Mack K.-H., Vigotti M., 1999, *A&A*, 345, 769
- O’Dea C. P., 1998, *PASP*, 110, 493
- O’Dea C. P., Baum S. A., 1997, *AJ*, 113, 148
- Pacholczyk A. G., 1970, *Radio astrophysics. Nonthermal processes in galactic and extragalactic sources*, Pacholczyk, A. G., ed.
- Parma P., Murgia M., Morganti R., Capetti A., de Ruiter H. R., Fanti R., 1999, *A&A*, 344, 7
- Randall K. E., Hopkins A. M., Norris R. P., Edwards P. G., 2011, *MNRAS*, 416, 1135
- Reichard T. A., Richards G. T., Schneider D. P., Hall P. B., Tolea A., Krolik J. H., Tsvetanov Z., Vanden Berk D. E., York D. G., Knapp G. R., Gunn J. E., Brinkmann J., 2003, *AJ*, 125, 1711
- Sanders D. B., Soifer B. T., Elias J. H., Neugebauer G., Matthews K., 1988, *ApJ*, 328, L35
- Silk J., Rees M. J., 1998, *A&A*, 331, L1
- Springel V., et al., 2005, *Nature*, 435, 629
- Trump J. R., Hall P. B., Reichard T. A., Richards G. T., Schneider D. P., Vanden Berk D. E., Knapp G. R., Anderson S. F., Fan X., Brinkman J., Kleinman S. J., Nitta A., 2006, *ApJS*, 165, 1
- Urrutia T., Becker R. H., White R. L., Glikman E., Lacy M., Hodge J., Gregg M. D., 2009, *ApJ*, 698, 1095
- Urrutia T., Lacy M., Becker R. H., 2008, *ApJ*, 674, 80
- Urrutia T., Lacy M., Gregg M. D., Becker R. H., 2005, *ApJ*, 627, 75
- White R. L., Helfand D. J., Becker R. H., Gregg M. D., Postman M., Lauer T. R., Oegerle W., 2003, *AJ*, 126, 706
- Wilkes B. J., Schmidt G. D., Cutri R. M., Ghosh H., Hines D. C., Nelson B., Smith P. S., 2002, *ApJ*, 564, L65